



Macromolecular crowding limits growth under pressure

Baptiste Alric¹, Cécile Formosa-Dague^{1,2}, Etienne Dague¹, Liam J. Holt³✉ and Morgan Delarue¹✉

Cells that grow in confined spaces eventually build up mechanical compressive stress. This growth-induced pressure decreases cell growth. Growth-induced pressure is important in a multitude of contexts, including cancer^{1–3}, microbial infections⁴ and biofouling⁵; yet, our understanding of its origin and molecular consequences remains limited. Here we combine microfluidic confinement of the yeast *Saccharomyces cerevisiae*⁶ with rheological measurements using genetically encoded multimeric nanoparticles⁷ to reveal that growth-induced pressure is accompanied with an increase in a key cellular physical property: macromolecular crowding. We develop a fully calibrated model that predicts how increased macromolecular crowding hinders protein expression and thus diminishes cell growth. This model is sufficient to explain the coupling of growth rate to pressure without the need for specific molecular sensors or signalling cascades. As molecular crowding is similar across all domains of life, this could be a deeply conserved mechanism of biomechanical feedback that allows environmental sensing originating from the fundamental physical properties of cells.

Cells in every kingdom of life can proliferate in spatially limited environments. In metazoans, tissues have physical boundaries⁸. In plants, roots sprout into solid ground^{9,10}. In microbes, substrate adhesion physically limits colony expansion^{11–13}. To proliferate in confinement, cells must push on the boundaries of their environment and neighbouring cells, leading to the development of compressive forces, which translates—at the multicellular scale—into the buildup of a mechanical growth-induced pressure (GIP). GIP decreases the rates of cell growth and division for all organisms: bacteria, fungi, plants or mammals^{1–3,5,14,15}. However, the mechanisms that control growth and proliferation under GIP remain unknown. In particular, it is unclear whether growth reduction is due to specific signalling pathways or is a necessary consequence of changes in the physical properties of cells.

Some signalling pathways have been associated with survival or division under GIP^{16,17}, but it remains unclear if these pathways affect growth per se. For example, mutants in the SCWISH network (composed of the cell-wall integrity pathway and signalling from Ste11 through Msb2/Sho1 proteins) tend to lyse due to mechanical instabilities associated with budding, but their ability to develop GIP is unperturbed¹⁷.

On the other hand, mechanical perturbations to cells also influence the fundamental physical parameters. One such parameter is macromolecular crowding, which relates to the high packing fraction of macromolecules in the cell, and can decrease the biochemical reaction rates due to decreased effective diffusion^{18–21}. However,

the role of crowding in response to mechanical stress in general, and GIP in particular, has been largely overlooked.

In this Letter, we investigated the relationship among GIP, macromolecular crowding and cell growth in the budding yeast *Saccharomyces cerevisiae*. Our results are best explained by a model in which the rates of intracellular osmolyte production and macromolecular biogenesis are intrinsically coupled. To develop GIP, osmolytes and macromolecules are produced, whereas cell expansion is limited, causing the cell interior to become crowded and leading to biophysical feedback that limits cell growth.

We used microfluidic elastic chambers as a model confining the three-dimensional (3D) environment (Fig. 1a and Extended Data Fig. 1a)⁶. After filling the chamber, the cells pushed against their neighbours and onto their surroundings. The cells were continually fed through microchannels to prevent nutrient depletion and enable the switching of media. After 10 h of confined growth, the elastic chamber was fairly deformed, almost doubling in volume. This deformation was used to measure the amount of GIP developed by the cells^{5,17}. We posited that under confinement, GIP resulted from an increase in intracellular osmotic pressure, which was balanced not only by the cell wall but also by the surrounding effective elasticity of the other cells and the polydimethylsiloxane (PDMS) chamber.

Remarkably, the cell size did not decrease as GIP increased (Fig. 1b), even though the cells became highly deformed (Fig. 1b, inset). The deformation of cells was a consequence of compressive forces. These forces can originate from an increase in the intracellular osmotic pressure that—due to confinement—applies forces to the chamber and to the surrounding cells, thereby deforming them, like inflating balloons inside a box (Fig. 1c, inset). Strikingly, we observed a strong reduction in the nuclear volume (Fig. 1c); as a result, the nuclear-to-cell volume ratio was perturbed. This is distinct from osmotic stress that leads to a proportional reduction in the nuclear volume, keeping the nuclear/cytoplasmic volume ratio constant²² (Extended Data Fig. 2).

We can subdivide osmolytes into two classes: small and large; we can operationally define them by their ability to freely diffuse across the nuclear pore at a cutoff value of the hydrodynamic radius of ~3 nm (ref. 23). The concentration of small osmolytes is dominated by ions and metabolites such as glycerol, whereas large osmolytes are macromolecules such as proteins, ribosomes and messenger RNA. The decrease in nuclear volume under osmotic stress is indicative of an increase in the concentration of cytoplasmic macromolecules. The changes in nuclear volume under GIP suggested that the concentration of cytoplasmic macromolecules was also increasing under GIP. In agreement, our data were best fit assuming that

¹LAAS-CNRS, Université de Toulouse, CNRS, Toulouse, France. ²TBI, Université de Toulouse, CNRS, INRAE, INSA, Toulouse, France. ³New York University Grossman School of Medicine, Institute for Systems Genetics, New York, NY, USA. ✉e-mail: liam.holt@nyulangone.org; morgan.delarue@laas.fr

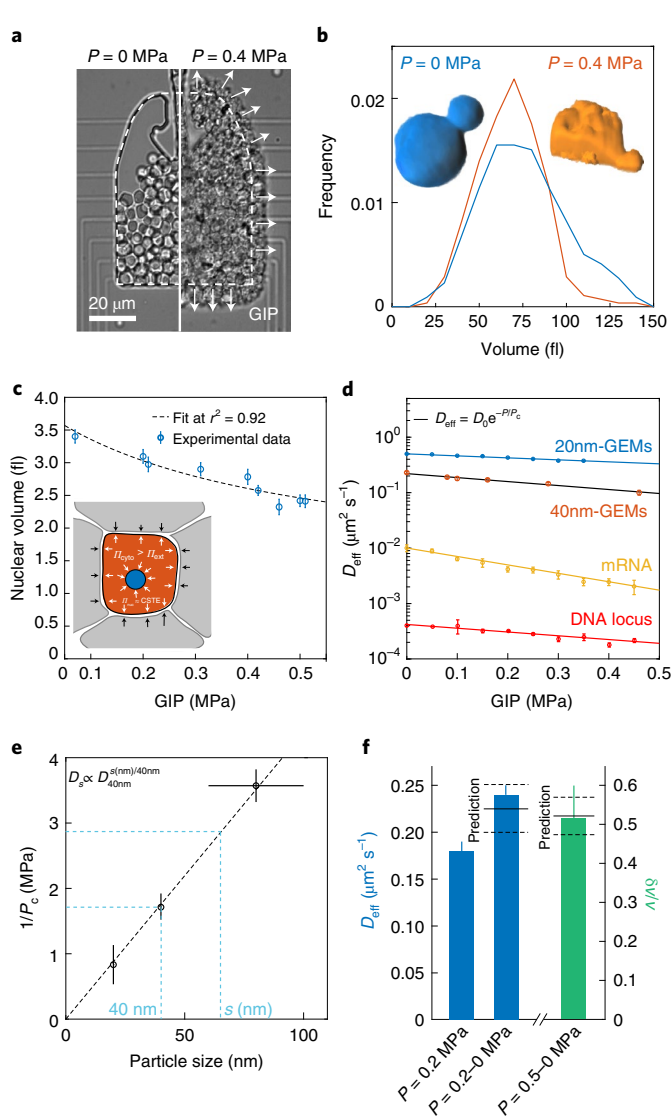


Fig. 1 | Confined growth leads to the intracellular accumulation of osmolytes and macromolecules. **a**, Confined growth leads to the buildup of GIP, measured by the deformation of the PDMS chamber. **b**, Cell volume distribution under GIP. Insets: representative 3D reconstructions of a non-compressed cell and a cell at 0.4 MPa. Both cells have a similar volume of ~ 65 fl. **c**, Nuclear volume decreases under GIP. Dashed line, fit of nuclear volume as a function of GIP assuming constant nuclear osmotic pressure ($r^2=0.92$). Π_{cytor} , Π_{ext} and Π_{nuc} are the cytosolic, external and nuclear osmotic pressures, respectively, and CSTE is a constant. **d**, Diffusivities of various particles and a DNA locus decrease exponentially as a function of GIP. The solid black curve is the model prediction for 40nm-GEMs ($r^2=0.98$). **e**, Characteristic pressure P_c of exponential dependence is inversely proportional to cytosolic particle size. **f**, After sudden pressure relaxation, effective diffusion rises quickly (<1 min) to control (uncompressed) values and cell volume increases (δv) due to the stored osmotic pressure. The predicted values are indicated. The diffusion data fall within 7% of the prediction, whereas the volume data fall within 2%. In all the data, the values are mean \pm standard error of the mean for $N \geq 3$ independent biological replicates.

these two osmolytes (small osmolytes and macromolecules) were increasing proportionally. Assuming that nuclear osmolarity did not adapt, we predicted that nuclear volume v_n would decrease with GIP, denoted as P (Supplementary Information):

$$\frac{\delta v_n}{v_n} = -\frac{P/\Pi_0}{1 + P/\Pi_0},$$

where Π_0 is the intracellular nominal ($P=0$ MPa) osmotic pressure and P corresponds to the surplus internal osmotic pressure above Π_0 . We fitted the nuclear volume data with $v_n = v_n^0 \left(1 + \frac{\delta v_n}{v_n}\right)$ ($r^2=0.92$) and obtained $\Pi_0 \approx 0.95 \pm 0.05$ MPa (Fig. 1c, dashed line). We measured the osmotic pressure of the culture medium at 30°C as $\Pi_c \approx 0.63$ MPa, leading to a nominal osmotic pressure difference between the cell interior and cell exterior as $\Delta \Pi \approx 0.30$ MPa, in agreement with values from the literature²⁴. Since the macromolecule concentration was increasing and cell volume remained constant, we predicted that macromolecular crowding would increase under GIP.

Changes in macromolecular crowding can be inferred by particle-tracking microrheology⁷. We recently developed genetically encoded multimeric nanoparticles (GEMs) as highly efficient tracer particles for microrheology⁷. The introduction of a gene that encodes a self-assembling scaffold protein tagged with a fluorescent protein generates cells that constitutively contain tracer particles of defined sizes. In this study, we used GEMs with a diameter of 20 nm (20nm-GEMs) and 40 nm (40nm-GEMs). These particles probe the mesoscale, that is, the length scale of multimeric macromolecular assemblies such as RNA polymerase and ribosomes.

Using probes of various sizes, we found that the increase in cytoplasmic crowding under mechanical compression strongly depended on the length scale (Fig. 1d): the effective diffusion of larger particles such as mRNA (~ 80 nm diameter²⁵) decreased far more than that of smaller particles such as 20nm-GEMs. We also found that the diffusion of a DNA locus decreased with GIP, probably as a consequence of decreased nuclear volume leading to increased nuclear crowding. Interestingly, the diffusivity of every tracer particle appeared to decay exponentially with increasing GIP, similar to previous observations *in vitro*¹⁹, and was more apparent for larger mRNA particles (Extended Data Fig. 3):

$$D = D_0 e^{-P/P_c},$$

where D_0 is the nominal diffusion of each particle, P is the GIP and P_c is the characteristic pressure of the exponential dependence on GIP for each particle. This exponential dependence of diffusion on GIP is theoretically predicted from the Doolittle relationship⁷ (Supplementary Information). However, as mentioned earlier, this prediction applies only if osmolytes and macromolecules maintain a fixed, proportional concentration. We found that $P_c \propto \Pi_0/\zeta$, where ζ is a constant related to the interactions of the nanoparticle with its surroundings. Using osmotic perturbations to instantaneously modify crowding (Extended Data Fig. 4), we were able to measure $P_c \approx 0.6$ MPa for 40nm-GEMs. Using this value, our theory accurately predicts the empirical data (in Fig. 1d, the solid black line is the prediction and the red dots are the data).

Experimentally, we found that P_c depends on the particle size, and was inversely proportional to the probe size s ($1/P_c = \beta s$, where β is the proportionality constant; Fig. 1e). This inverse relation implies that the effective cytosolic diffusion for a particle of any size s (in nanometres) is a power-law function of the diffusion at 40 nm: $D_s \propto e^{-\beta s P} = e^{-\beta s P \times \frac{40}{40}} = (e^{-40\beta P})^{\frac{s}{40}} \propto D_{40\text{nm}}^{s(nm)/40\text{nm}}$. Using this relationship, we can predict cytosolic diffusivity at any length scale from the effective diffusion of 40nm-GEMs ($D_{40\text{nm}}$).

Our data strongly suggest that confined growth leads to a concomitant increase in both internal osmotic pressure (leading to GIP and cell deformation) and macromolecular crowding (as evidenced by nuclear compaction and decreased nanoparticle diffusivity). Theory successfully predicts these observations if the increase in

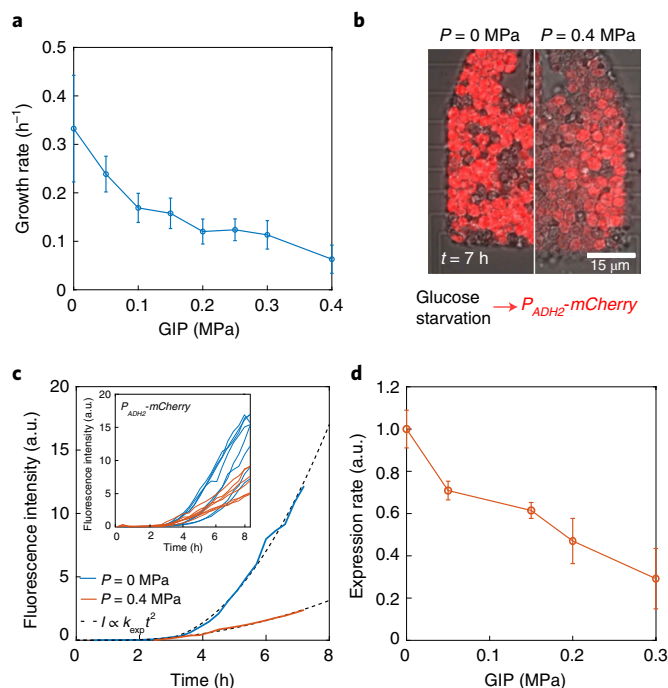


Fig. 2 | Confinement decreases growth and protein production rates.

a, Growth rate decays roughly exponentially with GIP. **b**, Representative images from the protein production reporter system. A reporter gene consisting of the *mCherry* fluorescent protein under the control of the *ADH2* promoter was integrated at the endogenous locus; glucose starvation induces the gene. After $t = 7$ h of induction, we observe stronger induction for the control (no pressure; left) condition than under GIP (right). **c**, Single-cell fluorescence intensities were fitted with a quadratic function (Methods) to extract the effective expression rate k_{exp} at various values of GIP. The representative curves for a single cell are shown with the fitting; multiple single-cell traces are shown in the inset. **d**, Protein expression rate decreases roughly exponentially with GIP. In all the data, values are mean \pm standard error of the mean for over $n \geq 100$ cells in $N \geq 3$ independent biological replicates.

GIP and crowding are proportional. Another prediction of this proportional coupling is that the relaxation of mechanical stress should lead to a cell volume increase proportional to GIP (Supplementary Information), that is, $\frac{\delta v}{v} = P/\Pi_0$, and for macromolecular crowding (and thus diffusivity) to reset to the nominal value without GIP. To test this prediction, we used a device in which GIP could be quickly relaxed (Extended Data Fig. 1b). Consistent with our model, we observed a fast, fully reversible and predictable increase in cell volume, as well as the recovery of GEMs diffusion on instantaneous relaxation of GIP (Fig. 1f). Together, this set of observations indicates that confined growth leads to a proportional increase in osmolyte and macromolecule concentration.

We next sought to investigate how GIP affects cell growth and protein production (which is dependent on the rates of multiple biochemical reactions). We first measured the changes in cell number and chamber volume to estimate the cellular growth rate (Methods and Extended Data Fig. 5). We observed that the growth rate decreased roughly exponentially with GIP (Fig. 2a). To get an insight into protein production, we used a fluorescent reporter assay. Protein production can take hours, raising the problem that GIP would continue to increase during the experiment if growth continued. To avoid this issue, we expressed the *mCherry* fluorescence protein from the *ADH2* promoter ($P_{\text{ADH2}}\text{-}m\text{Cherry}$) as our model system. The *ADH2* promoter is activated by glucose starvation,

a condition that also arrests cell growth²⁶. Thus, we could grow cells to develop a defined amount of GIP and then induce $P_{\text{ADH2}}\text{-}m\text{Cherry}$ by the withdrawal of glucose (osmotically balancing with sorbitol) within a range of GIP values. In this way, we could infer how protein expression, at least of this model gene, was affected by GIP. We observed that the induction of fluorescence signal was slower under GIP than in the control (Fig. 2b).

This experimental strategy enabled us to extract single-cell $P_{\text{ADH2}}\text{-}m\text{Cherry}$ fluorescence intensity curves. We observed that after an initial time delay, which could be associated with the sensing of carbon starvation or promoter remodelling, the fluorescence intensity increased with time and that this rate of increase was lower in compressed cells. We developed a mathematical model of transcription followed by translation to quantify the induction of fluorescence. Our model predicted that the protein concentration should increase quadratically with time at shorter timescales, with an effective rate k_{exp} that is the product of the transcription rate (k_m) and translation rate (k_p): $k_{\text{exp}} = k_m \times k_p$ (Supplementary Information). Although k_{exp} is not a rate (in the strict sense) but the product of two rates, we refer to it as a single effective rate hereafter, for the sake of simplicity.

Our simple model yielded an excellent fit to the experimental data (Fig. 2c), and enabled us to extract both time delay and k_{exp} . We observed that the time delay was progressively shorter with GIP (Extended Data Fig. 6). It has been previously shown that cells in the G1 phase of the cell cycle respond more rapidly to stress²⁶, and our previous studies showed that *S. cerevisiae* arrests in G1 in response to GIP^{5,17}. Therefore, the accumulation of cells in G1 could explain this reduced lag time under GIP. On the other hand, we found that k_{exp} decreased roughly exponentially with GIP (Fig. 2d), with a similar dependence as the growth rate decay (about 60% decrease at $P = 0.3$ MPa in both cases). We also observed a reduction in the protein production rate for the expression of a constitutively active $P_{\text{HIS3}}\text{-}GFP$ construct (GFP, green fluorescent protein), suggesting that this decrease in the rate of protein production was not restricted to the $P_{\text{ADH2}}\text{-}m\text{Cherry}$ gene (Extended Data Fig. 7).

Our microrheology data and nuclear compression demonstrated that macromolecular crowding increased under GIP. We hypothesized that this crowding could limit the protein expression rate and ultimately growth itself. This feedback could be physical as a result of decreases in the rate of diffusion-limited processes, with no need for specific signalling pathways. To test this idea, we set out to perturb molecular crowding by orthogonal means, using osmotic compression.

Increasing the external osmotic pressure, for example, by the addition of sorbitol to the media, leads to water efflux from cells, reducing the cell volume and increasing the concentration of biomolecules within the cell. This osmotic compression has previously been shown to increase macromolecular crowding¹⁸. Wild-type cells rapidly adapt to these perturbations through the osmotic response pathway, controlled by the Hog1p kinase, which increases the production of intracellular glycerol to counteract the increased external osmotic pressure. The rapid recovery from osmotic perturbation makes it difficult to interpret long-term experiments in wild-type cells. Furthermore, intracellular viscosity is affected by glycerol accumulation, making rheological measurements hard to interpret. To avoid these issues, we used *hog1Δ* mutant cells, which cannot rapidly adapt to acute osmotic stress²⁷. We, as well as others, find that *hog1Δ* cells can still expand and grow, even in the presence of increased concentrations of external osmolytes²⁸, indicating that the baseline generation of internal osmolytes persists²⁹. Therefore, at least two mechanisms generate intracellular osmolytes. First, a basal mechanism constitutively generates the osmotic pressure that cells require to expand and grow; we predict that this basal osmolyte production is coupled to the rate of macromolecule biosynthesis, but is not increased to allow cells to adapt to osmotic shock. Second, an

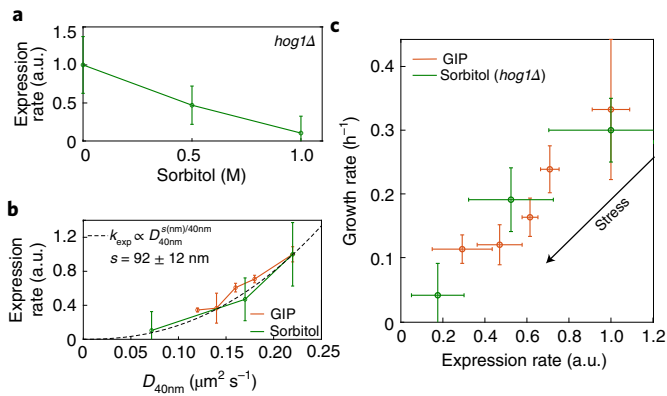


Fig. 3 | Protein production and growth are diffusion-limited processes.

a, Effective expression rate (k_{exp}) of P_{ADH2} -mCherry decreases under osmotic stress in $hog1\Delta$ cells. **b**, k_{exp} was fitted by a power-law function of the effective diffusion of 40nm-GEMs. **c**, Growth rate is proportional to protein production rate for $hog1\Delta$ cells under osmotic stress and wild-type cells under GIP. In all the data, the values are mean \pm standard error of the mean over $N \geq 3$ independent biological replicates.

acute stress response, dependent on Hog1p, allows cells to quickly adapt to changes in the external osmotic pressure.

We performed laser ablation experiments (Extended Data Fig. 8a) to confirm that $hog1\Delta$ cells still maintain the internal osmotic pressure, even after osmotic compression with 1 M sorbitol (Extended Data Fig. 8b). This experiment confirms that osmotic compression is a useful orthogonal approach that allows us to increase crowding at all the length scales, very similar to GIP. By using $hog1\Delta$ cells, we are able to maintain increased crowding for sufficient time to assess growth and protein expression rates.

We found that k_{exp} of P_{ADH2} -mCherry decreased with osmotic compression (Fig. 3a). If the effective expression rate (k_{exp}) of P_{ADH2} -mCherry is modulated by macromolecular crowding, then k_{exp} should display the same relationship to the effective diffusion of 40nm-GEMs (D_{40nm}) under both GIP and osmotic compression. Indeed, we observed the same dependence under both conditions (Fig. 3b), supporting the hypothesis that macromolecular crowding limits protein expression.

Our results are consistent with an effective protein expression rate that is diffusion limited at a certain unknown length scale, namely, D_{40nm} . We found that the relationship between the effective diffusion and particle diameter was a power law (Fig. 1e). If crowding decreases P_{ADH2} -mCherry production by inhibiting the diffusion of a rate-limiting particle, the effective expression rate should be a power-law function of D_{40nm} with an exponent that is the ratio of the particle size, s (in nanometres), divided by the size of the 40nm-GEMs (that is, 40 nm).

$$k_{exp} \propto D_s \propto D_{40nm}^{s(nm)/40nm}$$

Indeed, we observed this power-law dependence with an exponent suggesting that the expression was limited by the diffusion of particles of a characteristic size (s) of ~ 90 nm (Fig. 3b). This meso-scale length scale corresponds to many biological entities, for example, trafficking vesicles and mRNA ribonucleoprotein particles^{25,30,31} (both are ~ 100 nm). We note that if the process-limiting k_{exp} was nuclear or if multiple processes were to be limited, then the limiting size could be a little different (50–150 nm), but would remain in the mesoscale range.

We next investigated the hypothesis that the growth rate is mainly limited by protein expression. We plotted the growth rate

as a function of the effective expression rate of P_{ADH2} -mCherry and found that the two rates were roughly proportional. Note that this model gene is not limiting the growth rate as $ADH2$ is not expressed in the presence of glucose. Nevertheless, the fundamental processes required for its expression (for example, transcription by RNA polymerase II and translation by ribosomes) are shared by all the proteins. Interestingly, we observed that the same relationship held for both osmotic compression of $hog1\Delta$ cells and wild-type cells under GIP (Fig. 3c). Even osmotically compressed $hog1\Delta$ cells are able to grow. The fact that the growth rate similarly decreases with protein production under both osmotic stress and GIP indicates that similar limiting mechanisms could be at play.

Taking all of our results together, we developed a model of confined growth, with all the parameters experimentally determined, allowing us to predict the protein production and cell growth in confined conditions. The model derivation and parameterization are detailed in the Supplementary Information.

Our data support a central hypothesis that osmolyte and macromolecule production rates are tightly coupled. Exactly how this balance of rates is achieved remains unknown and is a long-standing fundamental question; however, as a consequence, in the absence of confinement, the cells grow and accumulate biomass as a constant level of macromolecular crowding is maintained. The accumulation of osmolytes increases the osmotic pressure. The mechanical balance between osmotic pressure and elastic properties of the cell wall, in turn, define the turgor pressure³². The turgor pressure enables the cell wall to expand through a process of hydrolysis and the insertion of new cell-wall material^{29,33}. We posit that the insertion of cell-wall material is only possible when the turgor pressure resulting from osmolyte accumulation is above a fixed value.

If the effective elasticity of the cell wall, encompassing the various mechanical parameters such as its Young modulus and Poisson ratio or thickness, were to increase (that is, require more force to be deformed), a higher pressure difference, and thus more osmolytes, would be required to achieve expansion. This is also the case during confined growth where the surroundings mechanically resist cell growth. Confined growth leads to an effective increase in the elasticity around the cell, which then physically limits cell-wall expansion (Fig. 4a). In our experiments, when cells fill the confining chamber and start to distort one another as well as the chamber walls, they experience an effective surrounding elasticity, E_{eq} . When the cells grow by δv , they need to accumulate more osmolytes to expand the cell wall, resulting in an increased internal pressure, which is the product of the surrounding effective elasticity and the volume change: $E_{eq} \times \delta v/v$. This value is the GIP. Based on our central hypothesis that the accumulation of osmolytes is proportionally coupled to the accumulation of macromolecular biomass, the decreased expansion rate will lead to increased macromolecular crowding. This increase in crowding then feeds back onto both protein and osmolyte production, which further reduces the cell expansion rate (Fig. 4a).

We calibrated the parameters related to our confining growth model, including the value of turgor pressure, using laser ablation, transmission electron microscopy and atomic force microscopy (AFM) (Methods and Extended Data Fig. 8a,c,d).

Our experimentally calibrated model accurately predicted the dependence of protein production and cell growth rate on pressure, as well as the dynamics of confined cell proliferation and GIP buildup, without any fitting of the free parameters (Fig. 4b–d, thick orange lines). This remarkable predictive power supports our simple model: growth is initially limited by the surrounding elastic environment, which forces the cell to increase the internal osmolarity. Osmolyte production is directly coupled to macromolecular biosynthesis, thereby leading to mesoscale crowding. High meso-scale intracellular crowding then physically inhibits the reactions through diffusion-limited processes. Our model shows that most of

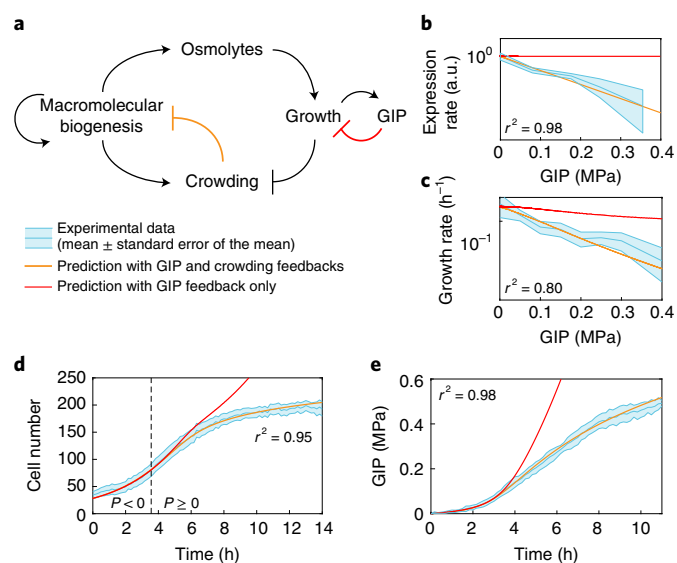


Fig. 4 | A physical feedback model in which crowding limits protein production and predicts the dynamics of confined cell growth.

a, Schematic of the model. After confluence is reached, GIP increases as a function of the cell volume change and the effective elasticity of the surrounding cells and PDMS chamber walls. The cells must accumulate more osmolytes to grow in the face of increasing effective elasticity; therefore, volume expansion is inhibited. Macromolecular biogenesis is proportionally coupled to osmolyte production; therefore, intracellular crowding increases. Increased mesoscale crowding feeds back onto many processes including the processes associated with macromolecule biogenesis itself, thereby limiting growth. **b–e**, Predictions of the dependence of various observables on GIP from the model. All the parameters are experimentally determined. The predictions are shown for the effective protein expression rate (**b**), growth rate (**c**), cell number (**d**) and GIP (**e**). In all the plots, the thick orange line represents the model prediction. The thick red line represents the prediction of the model without any physical (crowding) feedback on biomass production. The dashed line represents the onset of confluence and GIP buildup. The r^2 value indicates the square difference of the model against the data. The values are mean \pm standard error of the mean for $N \geq 3$ independent biological replicates.

the observed decrease in the growth rate can be explained by this physical feedback, without the need to evoke any other mechanism.

We also investigated the predictions of our model if we removed the physical feedback (Fig. 4b–d, thick red lines). In this case, GIP and cell number would rise much more quickly than experimentally observed. Growth would still ultimately decrease due to the increasing mechanical barrier to cell expansion, but much more slowly than observed because the rate of osmolyte production would not be limited. In this case, crowding would also rise quickly, and crowders in the cell would approach the maximum random close packing fraction much sooner. We speculate that the physical feedback of crowding on biosynthesis is adaptive, as it delays and attenuates macromolecular overcrowding, which could allow more time for stress responses to more efficiently activate. Which step of protein biosynthesis is limited by crowding is, however, unknown and requires a separate investigation.

An intriguing question is why cells have not evolved adaptive mechanisms to change the relative rates of macromolecular biosynthesis and osmolyte production to prevent overcrowding of the cell. The osmotic stress response is an adaptive mechanism of this type. However, we observed that GIP in *hog1Δ* mutants, which are defective for the osmotic stress pathway, was similar to that in

wild-type cells (Extended Data Fig. 9). A key difference between GIP and osmotic shock is the effect on turgor. The activation of the osmoadaptive HOG1 pathway in *S. cerevisiae* is linked with a loss of turgor³⁴. However, our results suggest that turgor does not decrease during GIP; in fact, it increases due to the effective elasticity of the surroundings, effectively acting like a thicker cell wall. Increased turgor actually triggers the hypo-osmotic stress response, which decreases intracellular osmolarity and subsequently the cell volume³⁵. However, this would be counterproductive during confined growth as a reduced cell volume would further increase crowding. Indeed, pathways related to the response to both hyper- and hypo-osmotic stress are triggered by GIP. These pathways, which together constitute the SCWISH network¹⁷, are important for cell survival under GIP, but they do not appear to change the coupling between the osmolyte and macromolecule biosynthesis. Perhaps, the feedback between mesoscale crowding and growth is useful: diffusion is affected with a strong size dependence, mainly limiting the reactions at the mesoscale (≥ 10 nm diameter). It is intriguing that many stress response proteins are relatively small. Therefore, on developing strong GIP, growth will stall, but stress response pathways can continue to operate.

Stress-response signalling pathways vary extensively between organisms. In contrast, high macromolecular crowding is a fundamental property of all life forms³⁶. Our results suggest that a primordial biophysical feedback mechanism directly arises from the physical properties of cells. This feedback could be essential for multicellular proliferation, and its deregulation is important in the context of some pathologies. In particular, cancer cells, in contrast with normal cells, acquire the capacity to proliferate under confinement and build up GIP¹, suggesting that genetic alterations, or chemical environmental modifications, can impact the ability to proliferate under confinement.

Online content

Any methods, additional references, Nature Research reporting summaries, source data, extended data, supplementary information, acknowledgements, peer review information; details of author contributions and competing interests; and statements of data and code availability are available at <https://doi.org/10.1038/s41567-022-01506-1>.

Received: 7 June 2021; Accepted: 6 January 2022;

Published online: 24 February 2022

References

- Helmlinger, G., Netti, P. A., Lichtenbeld, H. C., Melder, R. J. & Jain, R. K. Solid stress inhibits the growth of multicellular tumor spheroids. *Nat. Biotechnol.* **15**, 778–783 (1997).
- Alessandri, K. et al. Cellular capsules as a tool for multicellular spheroid production and for investigating the mechanics of tumor progression in vitro. *Proc. Natl Acad. Sci. USA* **110**, 14843–14848 (2013).
- Rizzuti, I. et al. Mechanical control of cell proliferation increases resistance to chemotherapeutic agents. *Phys. Rev. Lett.* **125**, 128103 (2020).
- Bonazzi, D. et al. Intermittent pili-mediated forces fluidize *Neisseria meningitidis* aggregates promoting vascular colonization. *Cell* **174**, 143–155.e16 (2018).
- Delarue, M. et al. Self-driven jamming in growing microbial populations. *Nat. Phys.* **12**, 762–766 (2016).
- Holt, L. J., Hallatschek, O. & Delarue, M. Mechano-chemostats to study the effects of compressive stress on yeast. *Methods Cell. Biol.* **147**, 215–231 (2018).
- Delarue, M. et al. mTORC1 controls phase separation and the biophysical properties of the cytoplasm by tuning crowding. *Cell* **174**, 338–349.e20 (2018).
- Streichan, S. J., Hoerner, C. R., Schneid, T., Holzer, D. & Hufnagel, L. Spatial constraints control cell proliferation in tissues. *Proc. Natl Acad. Sci. USA* **111**, 5586–5591 (2014).
- Bengough, A. G., Croser, C. & Pritchard, J. A biophysical analysis of root growth under mechanical stress. *Plant Soil* **189**, 155–164 (1997).
- Fal, K. et al. Tissue folding at the organ–meristem boundary results in nuclear compression and chromatin compaction. *Proc. Natl Acad. Sci. USA* **118**, e2017859118 (2021).

11. Rivera-Yoshida, N., Arias Del Angel, J. A. & Benítez, M. Microbial multicellular development: mechanical forces in action. *Curr. Opin. Genet. Dev.* **51**, 37–45 (2018).
12. Asally, M. et al. Localized cell death focuses mechanical forces during 3D patterning in a biofilm. *Proc. Natl Acad. Sci. USA* **109**, 18891–18896 (2012).
13. Trejo, M. et al. Elasticity and wrinkled morphology of *Bacillus subtilis* pellicles. *Proc. Natl Acad. Sci. USA* **110**, 2011–2016 (2013).
14. Stewart, P. S. & Robertson, C. R. Microbial growth in a fixed volume: studies with entrapped *Escherichia coli*. *Appl. Microbiol. Biotechnol.* **30**, 34–40 (1989).
15. Chu, E. K., Kilic, O., Cho, H., Groisman, A. & Levchenko, A. Self-induced mechanical stress can trigger biofilm formation in uropathogenic *Escherichia coli*. *Nat. Commun.* **9**, 4087 (2018).
16. Nam, S. et al. Cell cycle progression in confining microenvironments is regulated by a growth-responsive TRPV4-PI3K/Akt-p27^{Kip1} signaling axis. *Sci. Adv.* **5**, eaaw6171 (2019).
17. Delarue, M. et al. SCWISH network is essential for survival under mechanical pressure. *Proc. Natl Acad. Sci. USA* **114**, 13465–13470 (2017).
18. Miermont, A. et al. Severe osmotic compression triggers a slowdown of intracellular signaling, which can be explained by molecular crowding. *Proc. Natl Acad. Sci. USA* **110**, 5725–5730 (2013).
19. Vibhute, M. A. et al. Transcription and translation in cytomimetic protocells perform most efficiently at distinct macromolecular crowding conditions. *ACS Synth. Biol.* **9**, 2797–2807 (2020).
20. Nettesheim, G. et al. Macromolecular crowding acts as a physical regulator of intracellular transport. *Nat. Phys.* **16**, 1144–1151 (2020).
21. Fernandez-De-Cossio-Díaz, J. & Vazquez, A. A physical model of cell metabolism. *Sci. Rep.* **8**, 8349 (2018).
22. Petelenz-Kurdtziel, E. et al. Quantification of cell volume changes upon hyperosmotic stress in *Saccharomyces cerevisiae*. *Integr. Biol.* **3**, 1120–1126 (2011).
23. Görlich, D. & Kutay, U. Transport between the cell nucleus and the cytoplasm. *Annu. Rev. Cell Dev. Biol.* **15**, 607–660 (2003).
24. de, I. M., Marechal, P.-A. & Gervais, P. Passive response of *Saccharomyces cerevisiae* to osmotic shifts: cell volume variations depending on the physiological state. *Biochem. Biophys. Res. Commun.* **227**, 519–523 (1996).
25. Borodavka, A. et al. Sizes of long RNA molecules are determined by the branching patterns of their secondary structures. *Biophys. J.* **111**, 2077–2085 (2016).
26. Busti, S., Coccetti, P., Alberghina, L. & Vanoni, M. Glucose signaling-mediated coordination of cell growth and cell cycle in *Saccharomyces cerevisiae*. *Sensors* **10**, 6195–6240 (2010).
27. Tamás, M. J. & Hohmann, S. The osmotic stress response of *Saccharomyces cerevisiae*. in *Yeast Stress Responses. Topics in Current Genetics* Vol. 1 (eds Hohmann S. & Mager W. H.) 121–200 (Springer, 2003).
28. Maayan, I. & Engelberg, D. The yeast MAPK Hog1 is not essential for immediate survival under osmostress. *FEBS Lett.* **583**, 2015–2020 (2009).
29. Rojas, E. R., Huang, K. C. & Theriot, J. A. Homeostatic cell growth is accomplished mechanically through membrane tension inhibition of cell-wall synthesis. *Cell Syst.* **5**, 578–590.e6 (2017).
30. Puchner, E. M., Walter, J. M., Kasper, R., Huang, B. & Lim, W. A. Counting molecules in single organelles with superresolution microscopy allows tracking of the endosome maturation trajectory. *Proc. Natl Acad. Sci. USA* **110**, 16015–16020 (2013).
31. Takamori, S. et al. Molecular anatomy of a trafficking organelle. *Cell* **127**, 831–846 (2006).
32. Vella, D., Ajdari, A., Vaziri, A. & Boudaoud, A. The indentation of pressurized elastic shells: from polymeric capsules to yeast cells. *J. R. Soc. Interface* **9**, 448–455 (2012).
33. Albersheim, P., Darvill, A., Roberts, K., Sederoff, R. & Staehelin A. *Plant Cell Walls* (Garland Science, 2010).
34. Schaber, J. et al. Biophysical properties of *Saccharomyces cerevisiae* and their relationship with HOG pathway activation. *Eur. Biophys. J.* **39**, 1547–1556 (2010).
35. Levin, D. E. Cell wall integrity signaling in *Saccharomyces cerevisiae*. *Microbiol. Mol. Biol. Rev.* **69**, 262–291 (2005).
36. Ellis, R. J. Macromolecular crowding: obvious but underappreciated. *Trends Biochem. Sci.* **26**, 597–604 (2001).

Publisher's note Springer Nature remains neutral with regard to jurisdictional claims in published maps and institutional affiliations.

© The Author(s), under exclusive licence to Springer Nature Limited 2022

Methods

Cell culture conditions. Cells were cultured on a synthetic complete (SC) medium (with 20 g l^{-1} glucose) agar Petri dishes, and resuspended 24 h before the experiment in a liquid medium at 30°C . The cells were then loaded into the microfluidic chamber (optical density, $\text{OD} \approx 0.3$). All the strains used in this study were fabricated in the laboratory of L. Holt, except the *Nup47-mCherry* strain kindly provided by A. Taddei (Institut Curie). A complete table of the strains used in this study is available in the Supplementary Information.

Induction of osmotic stress. Sorbitol is commonly used to induce osmotic stress in *S. cerevisiae*, as it increases the osmolarity of the culture medium, whereas its metabolism is negligible in the presence of glucose. Note that synthetic complete dextrose contains many permeable osmolytes, such as amino acids and glucose. Thus, intracellular concentration is likely to participate in intracellular osmolarity. However, they remain in large excess in the culture medium and their import is unlikely to impact the estimation of the difference in osmotic pressure.

Thus, to induce osmotic stress, sorbitol was added to the SC medium to induce osmotic shocks. The cells were then flowed into an Ibidi μ -slide VI coated with concanavalin A (Sigma-Aldrich) to promote cell attachment.

Microfabrication of PDMS devices. Moulds were created in a clean room in LAAS-CNRS, through classical photolithography on epoxy resin SU8 (Microchem) to create two layers: one at a height of $0.8\ \mu\text{m}$, defining the nutrient channels (SU8 2000.5); the other at a height of $10\ \mu\text{m}$, defining the cell growth chamber and the main cell-loading channel (SU8 3005). The moulds were treated with silane to limit interactions between the mould and PDMS.

SYLGARD 184 was mixed at a ratio of 1:10 (curing agent:base) and poured on the mould to reticulate overnight at 60°C . After this step, PDMS was cut, punched and cleaned with isopropanol to create microfluidic chips that were bound to glass coverslips by plasma binding (Diener PICO; gas, oxygen; pressure, $0.3\ \text{mbar}$; power, 100%; activation, 30 s) and then cured in an oven for $\geq 5\ \text{h}$.

Microfluidic device operation. To avoid bubbles, the chambers were filled in a precise sequence: first, the cell suspension was put inside the chambers and then the main channel was filled with the SC medium. A Fluigent MFCS pressure controller flowed the SC medium into the chips at a pressure of $\sim 1.5\ \text{bar}$ during all the experiments. The chips were placed within the thermoregulated microscope chamber at 30°C (Leica TempControl 37).

Image acquisition. The experiments were performed on a Leica DM IRB microscope with spinning-disk confocal scanner unit (Yokogawa CSU-X1) with a nominal power of $100\ \text{mW}$ and a Hamamatsu scientific complementary metal-oxide-semiconductor camera (ORCA-Flash4.0). For fluorescence acquisition, we used several emission filters, namely, ET450/50m (DAPI), ET525/50m (GFP) and ET595/50m (red), as well as a dichroic mirror (ZT405/488/561/640rpc, Chroma). All the acquisitions used $\times 63$ objective.

Deformation of PDMS chambers, measured by bright-field microscopy, was used to infer the GIP. The relationship between pressure and chamber deformation was calibrated as done elsewhere¹⁷, giving a value of $6.8\ \mu\text{m MPa}^{-1}$.

The number of cells was determined by counting the nuclei every 15 min, detected using an *HTB2-mCherry* fluorescent histone marker and using a $561\ \text{nm}$ laser (20% power and 100 ms exposure). The P_{ADH2} reporter was detected using the same acquisition parameters.

Single-particle tracking. Various methods could be used to assess intracellular crowding. We chose to use single-particle tracking of nanoparticles because this approach allows the rapid estimation of crowding from the diffusion coefficient of nanoparticles, does not require calibration (in contrast with fluorescence correlation spectroscopy) and is insensitive to changes in the chemical environment (unlike Förster resonance energy transfer-based sensors). Moreover, it reports on crowding at the scale of tens of nanometres, which is the relevant scale for the diffusion of large protein complexes.

GEMs, mRNPs and DNA locus videos were acquired by illumination with a $488\ \text{nm}$ laser at full power. Thirty images were acquired with no delay of continual exposure at a frame rate of $100\ \text{Hz}$ for GEMs and $10\ \text{Hz}$ for mRNPs. The DNA locus was illuminated for 100 ms and imaged every second. Particle tracking was achieved with FIJI MosaicSuite (v. 1.0.24)³⁷ and analysed with a home-made MATLAB (v. 2020a) script.

Nuclear and cell volume measurement. We took Z stacks (step, $0.3\ \mu\text{m}$) of cytosolic GFP and nuclear-envelope-tagged cells for volume measurement. The projection of the nuclear envelope was followed by a circular Hough analysis in MATLAB to extract the radii of the largest circles corresponding to the radii of nuclei in both osmotic stress and GIP experiments. Threshold-based segmentation was used to obtain the cell contour under osmotic stress as well as allow for 3D reconstruction and cell volume measurement. However, because of the tight cellular packing, automated cell segmentation and reconstruction was challenging for the GIP data. We, therefore, manually segmented the cells to measure the cell

volume. This measurement was independently performed by B.A. and M.D., and the obtained data were mixed together to limit potential biases.

Glucose starvation experiments to induce P_{ADH2} -mCherry. To induce the P_{ADH2} -mCherry reporter, cells were allowed to build up GIP in synthetic complete dextrose in the microfluidic devices overnight. Then, the culture medium inside the main channel was flushed and replaced by an SC medium without glucose but supplemented with $200\ \text{mM}$ sorbitol to balance the osmolarity. Note that only about 2% difference in fluorescence intensity was measured in the centre versus the edge of the chamber (Extended Data Fig. 10), suggesting that the nutrient conditions were similar throughout the device.

Laser ablation experiments. Cell ablation was performed on an Olympus BX51WI upright microscope equipped with a swept-field confocal microscope (Bruker) and a Ti:sapphire two-photon Chameleon Ultra II laser (Coherent). Cell autofluorescence was visualized using a $405\ \text{nm}$ laser, and ablation was performed using the two-photon laser at $770\ \text{nm}$. Images were acquired using an Olympus $\times 60/1.0$ objective and an electron-multiplying charge-coupled device camera (Photometrics). The experiment was set up and performed using the Prairie View software. For each experiment, a region of interest was drawn over the cell and a time lapse was set to 30 frames at a frame rate of $0.95\ \text{s}$. Ablation was performed after the second image using three consecutive pulses of $20\ \text{ms}$ exposure.

Transmission electron microscopy experiments. The cells were prepared and imaged following the protocol detailed elsewhere³⁸. Briefly, $15\ \text{ml}$ yeast culture (OD measured at $600\ \text{nm}$, 0.5) was pelleted and resuspended in 2.5% glutaraldehyde in $0.1\ \text{M}$ sodium cacodylate buffer ($\text{pH}\ 7.2$) for $2\ \text{h}$ at room temperature and then stored at 4°C overnight. The cells were then spun down at $1,000\ \text{g}$, washed with sodium cacodylate buffer, treated with freshly prepared 1% sodium metaperiodate for $1\ \text{h}$, and then stained with 1% osmium tetroxide and 1.5% ferrocyanide for $1\ \text{h}$ at 4°C . The cells were embedded in 2% agar, dehydrated in a graded series of ethanol, infiltrated with propylene oxide/EMbed 812 mixtures and embedded in EMbed 812 resin (Electron Microscopy Sciences). Further, $70\ \text{nm}$ ultrathin sections were cut and mounted on $200\ \text{mesh}$ copper grids. The grids were stained with 6% uranyl acetate for $30\ \text{min}$ and lead citrate for $2\ \text{min}$ and then imaged with a Philips CM12 electron microscope (FEI) and photographed with a Gatan (resolution, $4,000 \times 2,700$) digital camera.

AFM experiments. AFM measurements were performed in a synthetic complete dextrose culture medium at a controlled temperature of 30°C using a JPK NanoWizard 3 AFM instrument (Bruker). MLCT AUWH cantilevers (Bruker) with spring constants of 0.59 and $0.38\ \text{N m}^{-1}$ were calibrated using the thermal noise method³⁹. Yeast cells were immobilized on surfaces coated with concanavalin A. Force measurements were recorded in the force spectroscopy mode using applied forces of 1.5 and $2.0\ \text{nN}$, an approach/retract speed of $1\ \mu\text{m s}^{-1}$ and a z length of $0.5\ \mu\text{m}$. Force maps of 20×20 force curves were recorded on areas of $1 \times 1\ \mu\text{m}^2$ on top of the cells. Cell spring constants were then calculated from the fit of the force curves to Hooke's law using the JPK data processing software (Bruker).

Data availability

Source data are available for this paper. All other data that support the plots within this paper and other findings of this study are available from the corresponding authors upon reasonable request.

Code availability

All the codes used in this paper are available from the corresponding authors upon reasonable request.

References

37. Sbalzarini, I. F. & Koumoutsakos, P. Feature point tracking and trajectory analysis for video imaging in cell biology. *J. Struct. Biol.* **151**, 182–195 (2005).
38. Griffith, J., Mari, M., De Mazière, A. & Reggiori, F. A cryosectioning procedure for the ultrastructural analysis and the immunogold labelling of yeast *Saccharomyces cerevisiae*. *Traffic* **9**, 1060–1072 (2008).
39. Hutter, J. L., & Bechhoefer, J. Calibration of atomic-force microscope tips. *Rev. Sci. Instrum.* **64**, 1868 (1993).

Acknowledgements

We thank E. Kassianidou for the initial help with the laser ablation experiments. We thank A. Liang, C. Petzold and K. Dancel-Manning at the NYULH DART Microscopy Laboratory for consultation and assistance with the transmission electron microscopy work; this core is partially funded by the NYU Cancer Center Support Grant NIH/NCI P30CA016087. The technological realizations and associated research works were partly supported by the French RENATECH network (M.D.). L.J.H. was funded by NIH grants R01 GM132447 and R37 CA240765, the American Cancer Society, the Pershing Square

Sohn Cancer Research Award and Chan Zuckerberg Initiative. We thank E. Rojas for fruitful discussions. L.J.H. and M.D. thank the FACE foundation for travel support.

Author contributions

B.A. and M.D. designed and performed the experiments and data analysis. C.F.-D. and E.D. performed the AFM experiments. L.J.H. designed the strains used in the study. B.A., L.J.H. and M.D. wrote the manuscript.

Competing interests

The authors declare no competing interests.

Additional information

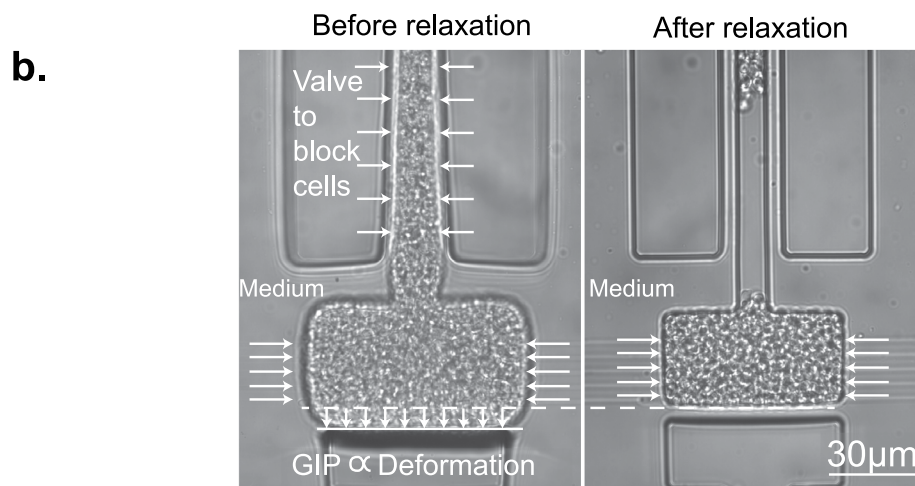
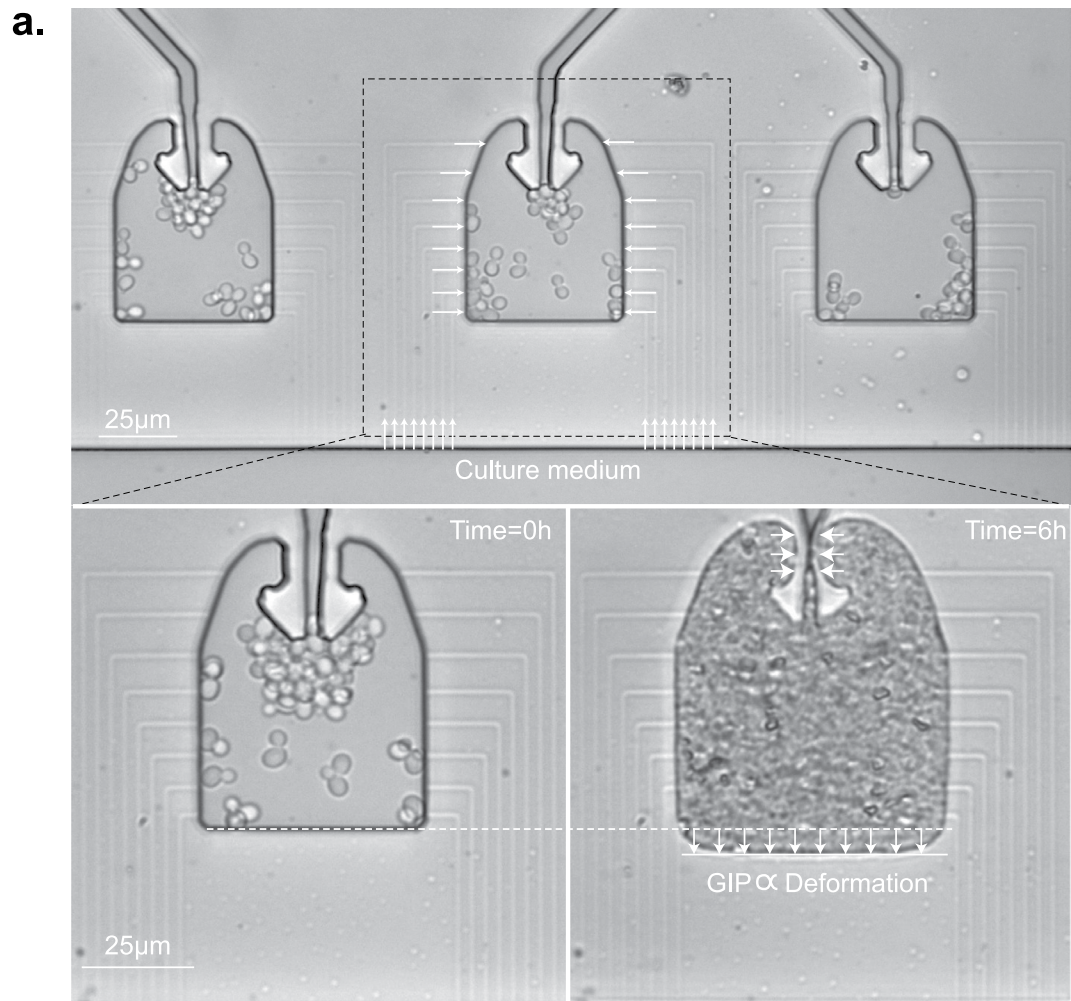
Extended data is available for this paper at <https://doi.org/10.1038/s41567-022-01506-1>.

Supplementary information The online version contains supplementary material available at <https://doi.org/10.1038/s41567-022-01506-1>.

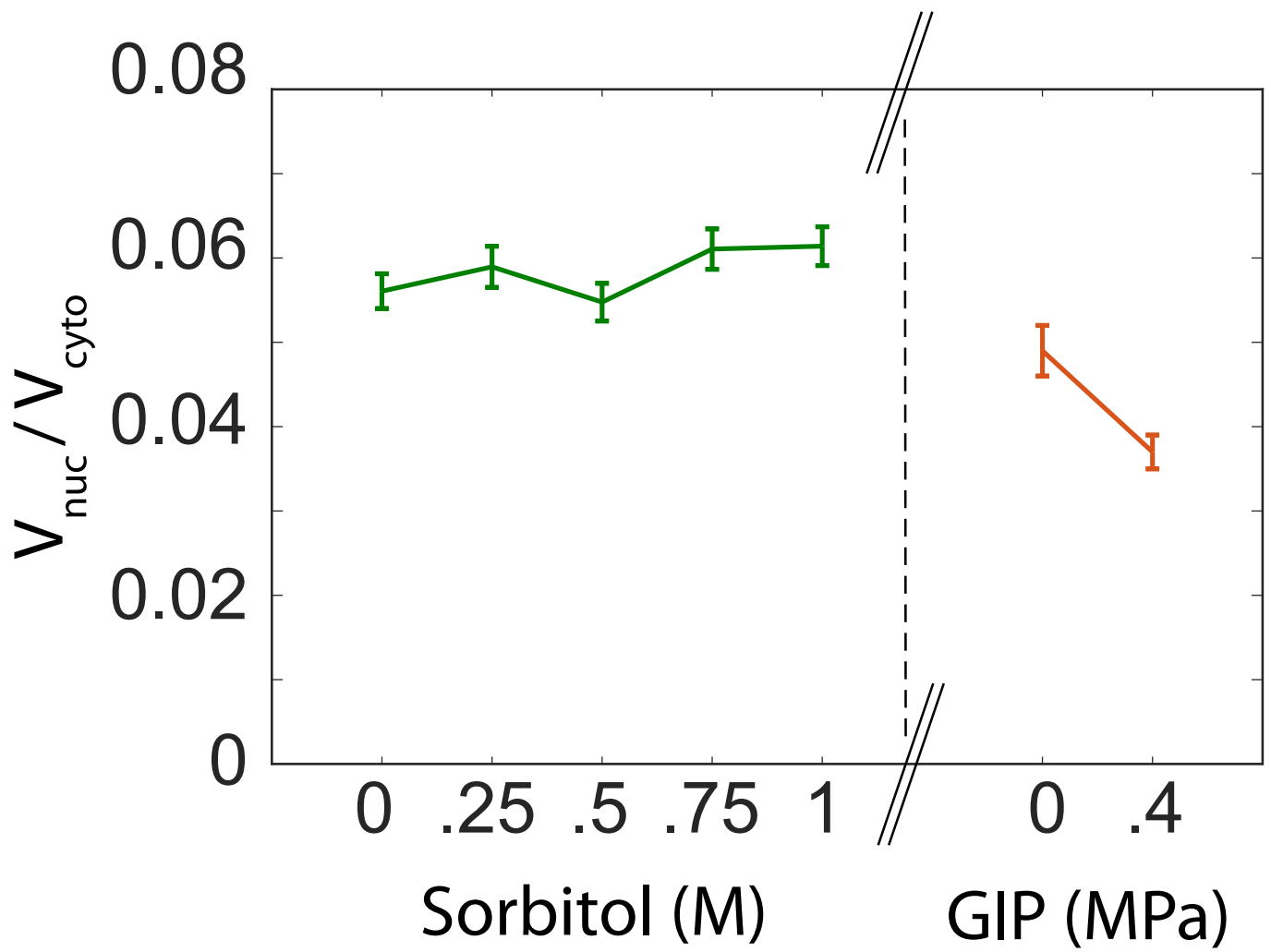
Correspondence and requests for materials should be addressed to Liam J. Holt or Morgan Delarue.

Peer review information *Nature Physics* thanks Pascal Hersen and the other, anonymous, reviewer(s) for their contribution to the peer review of this work.

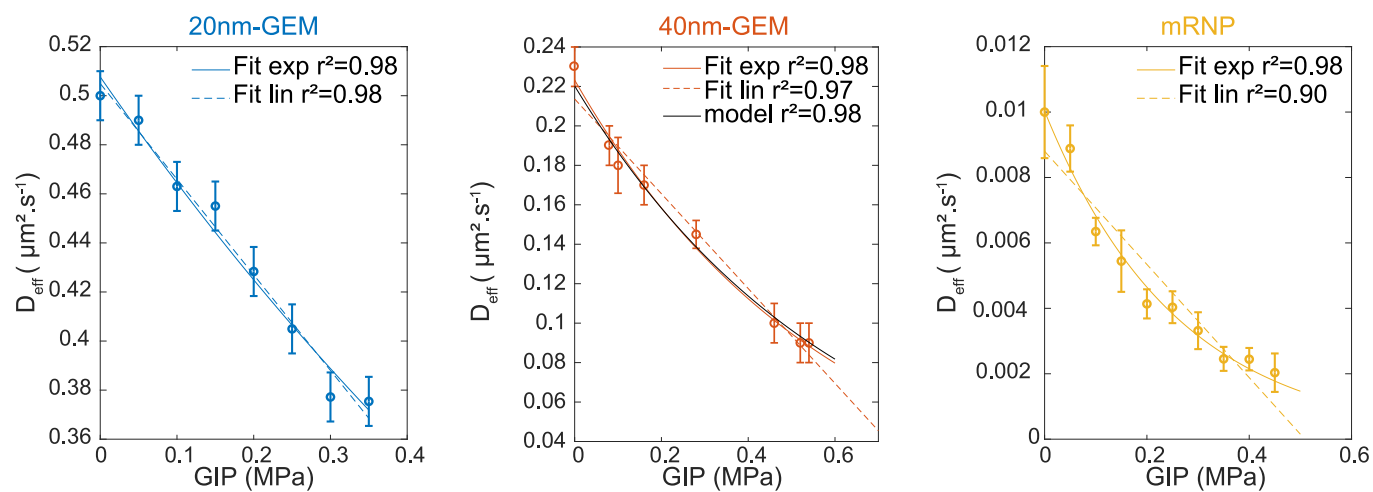
Reprints and permissions information is available at www.nature.com/reprints.



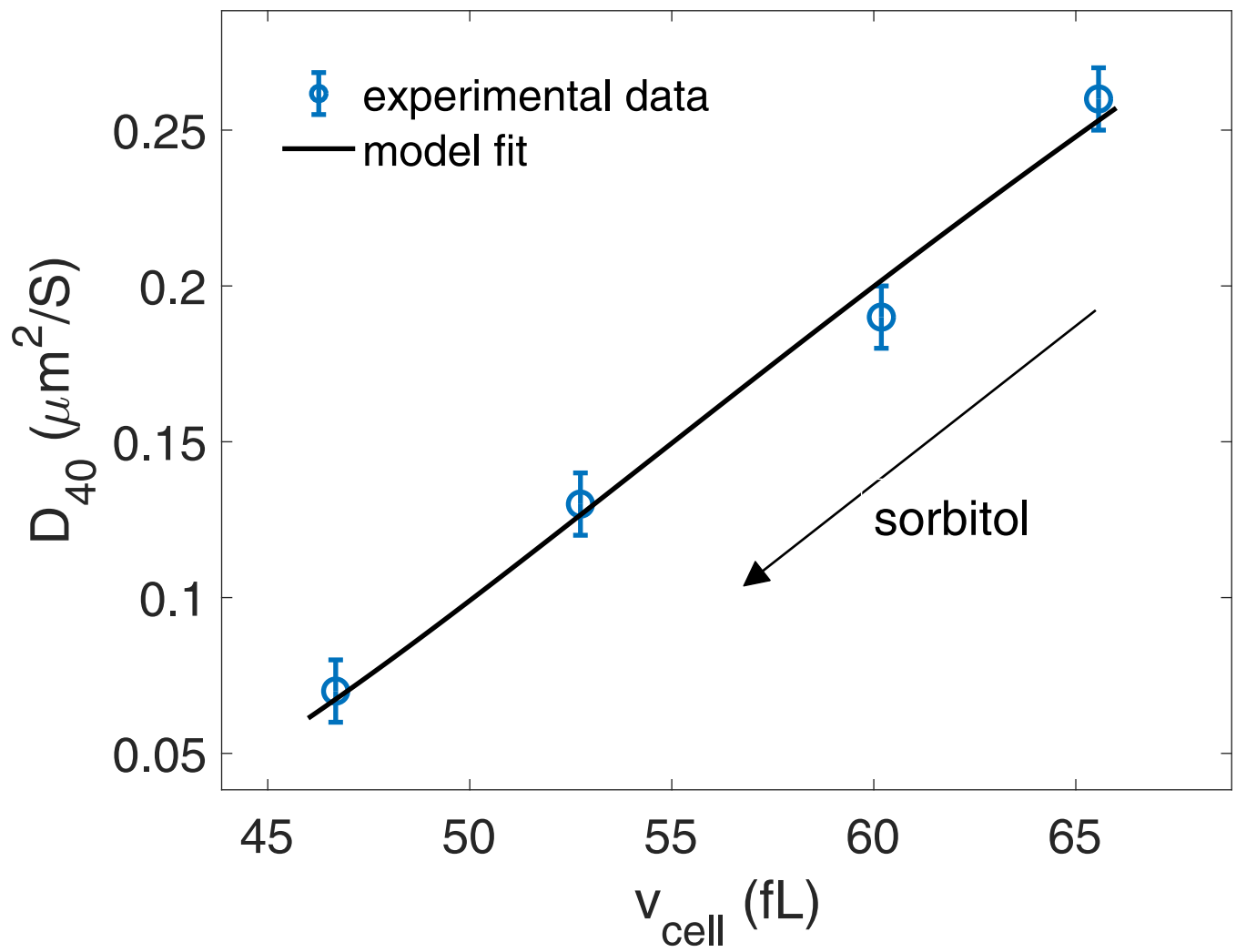
Extended Data Fig. 1 | Device used in the microfluidic experiments. a. Cells are loaded in a culture chamber connected on its sides to narrow channels that are used to set the chemical environment. Confined growth lead to the buildup of GIP, which is measured through the deformation of the elastic chamber. **b.** The culture chamber is, similar to the device presented in **a.**, connected to a set of narrow channels to set the chemical environment. A valve is actuated to confine the cell population and allow it to build up GIP. We estimate GIP by measuring the deformation of the PDMS membrane. Opening of the valve leads to a relaxation of GIP.



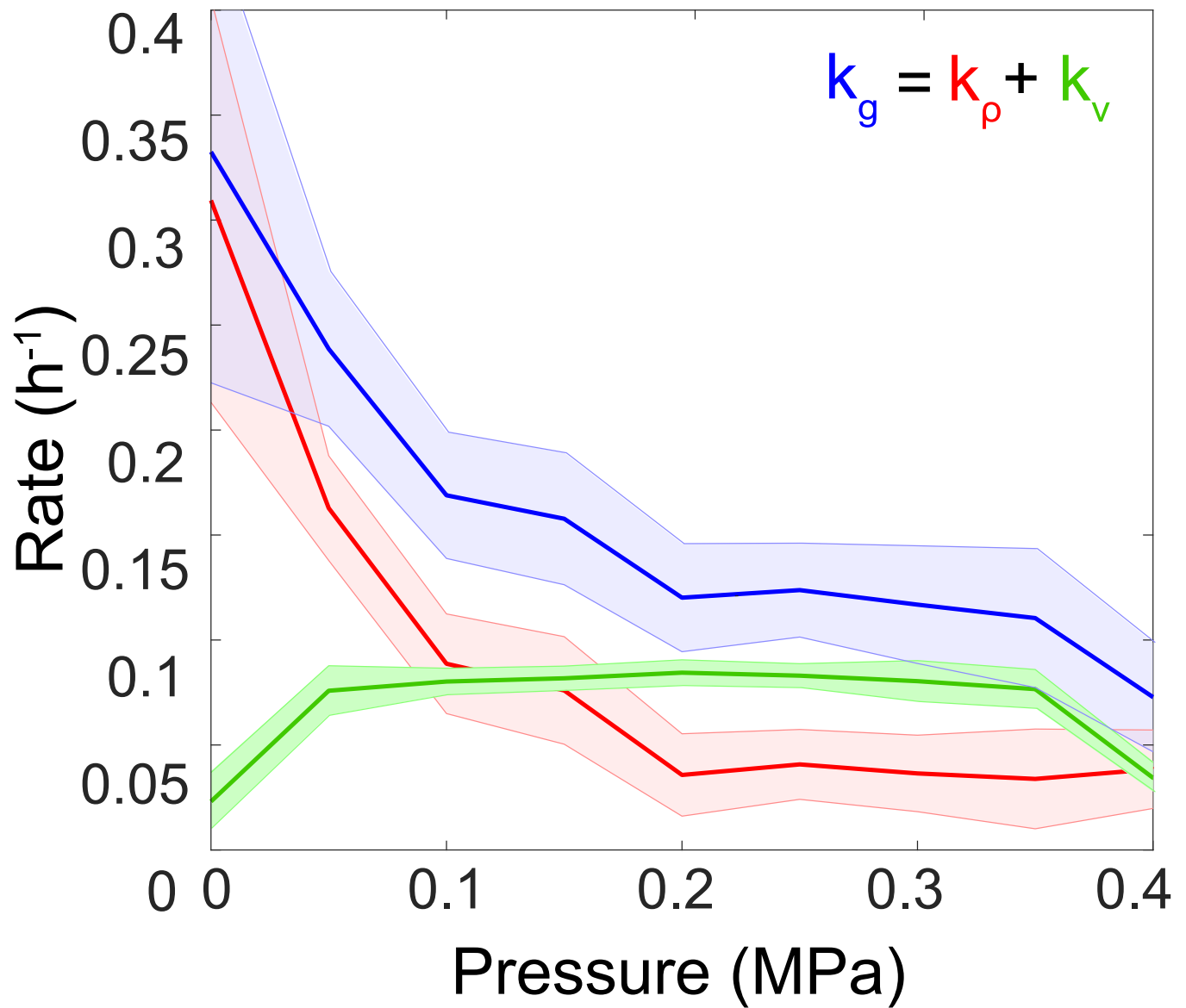
Extended Data Fig. 2 | Impact of osmotic shock. Ratio of nucleus and cytoplasm volume under osmotic shock and growth induced pressure.



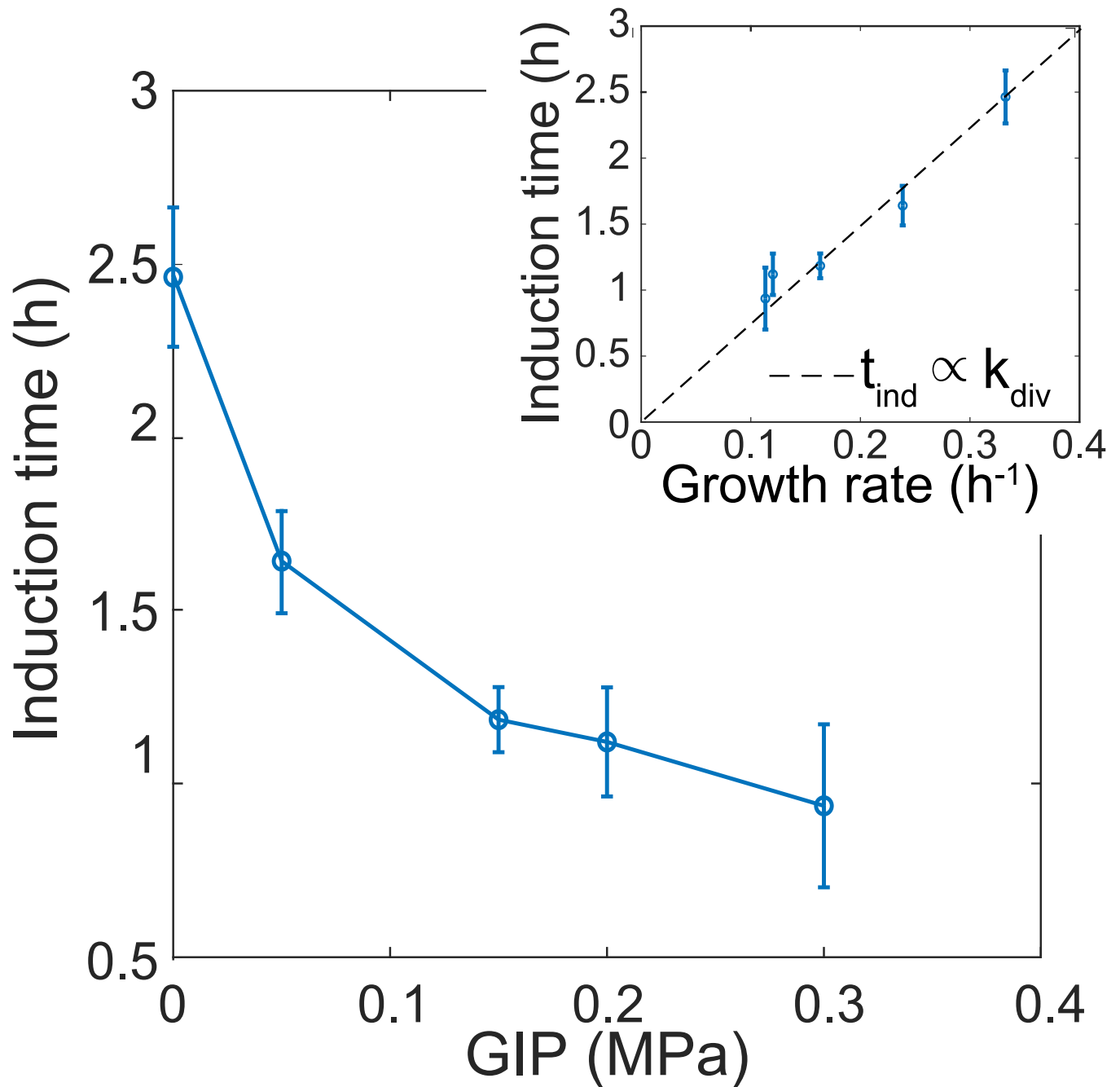
Extended Data Fig. 3 | Linear and exponential fits on the diffusion as a function of GIP data. The score for each fit is presented. We superimposed the prediction of diffusion as a function of GIP for the 40nm-GEMs, as well as the corresponding score.



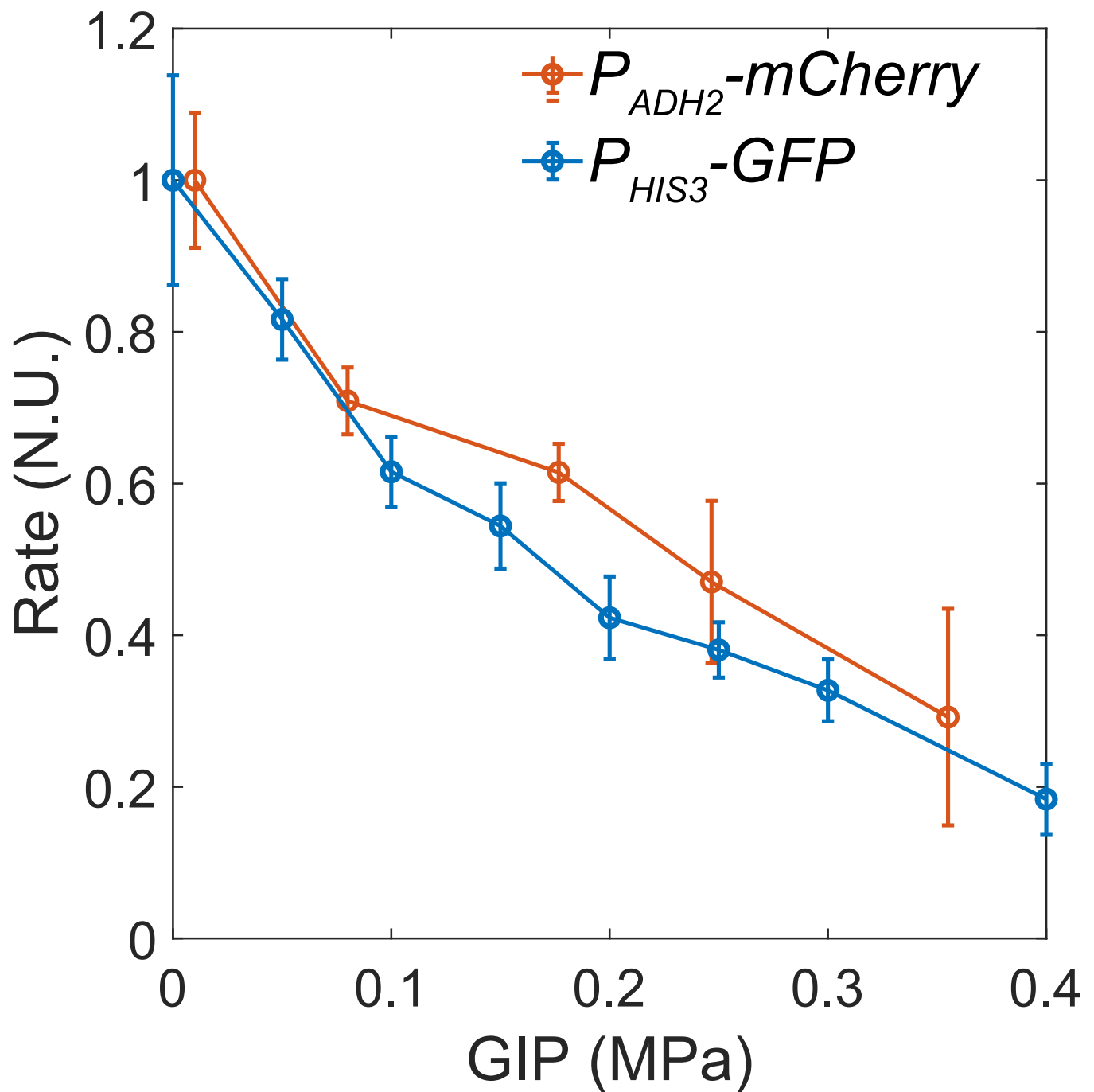
Extended Data Fig. 4 | 40nm-GEMs diffusion as a function of cell volume. Model fit (Eq. (13)) of the experimental data to extract $\xi_{40} = 7.4 \pm 2.5$ ($r^2 = 0.99$).



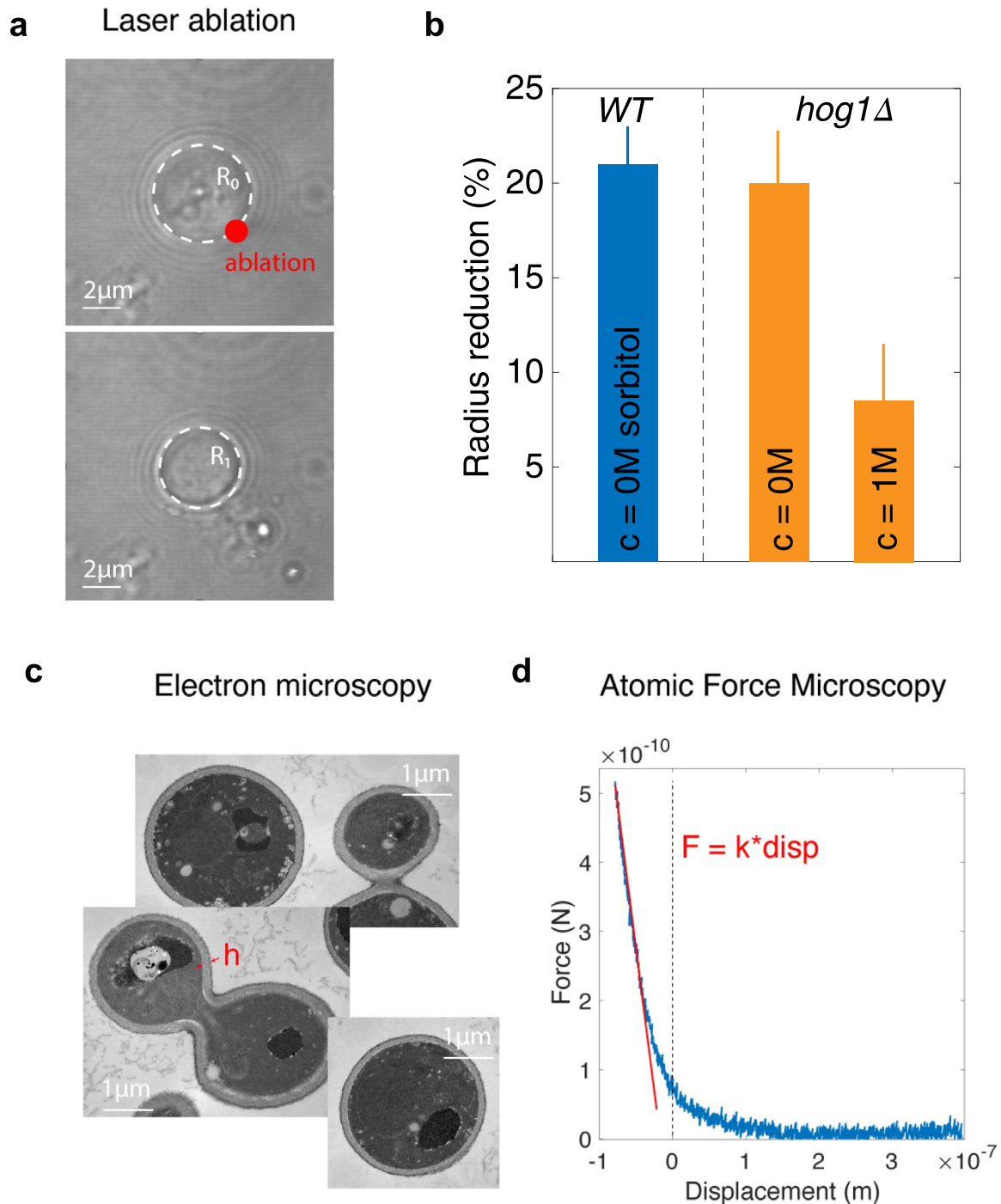
Extended Data Fig. 5 | Contribution of density and chamber volume change in the growth rate. For simplicity, we denoted k_g as the growth rate, $k_\rho = \partial_t \rho / \rho$ as the contribution of cell density ρ to growth rate, and $k_v = \partial_t V / V$ the contribution of the volume of the chamber V .



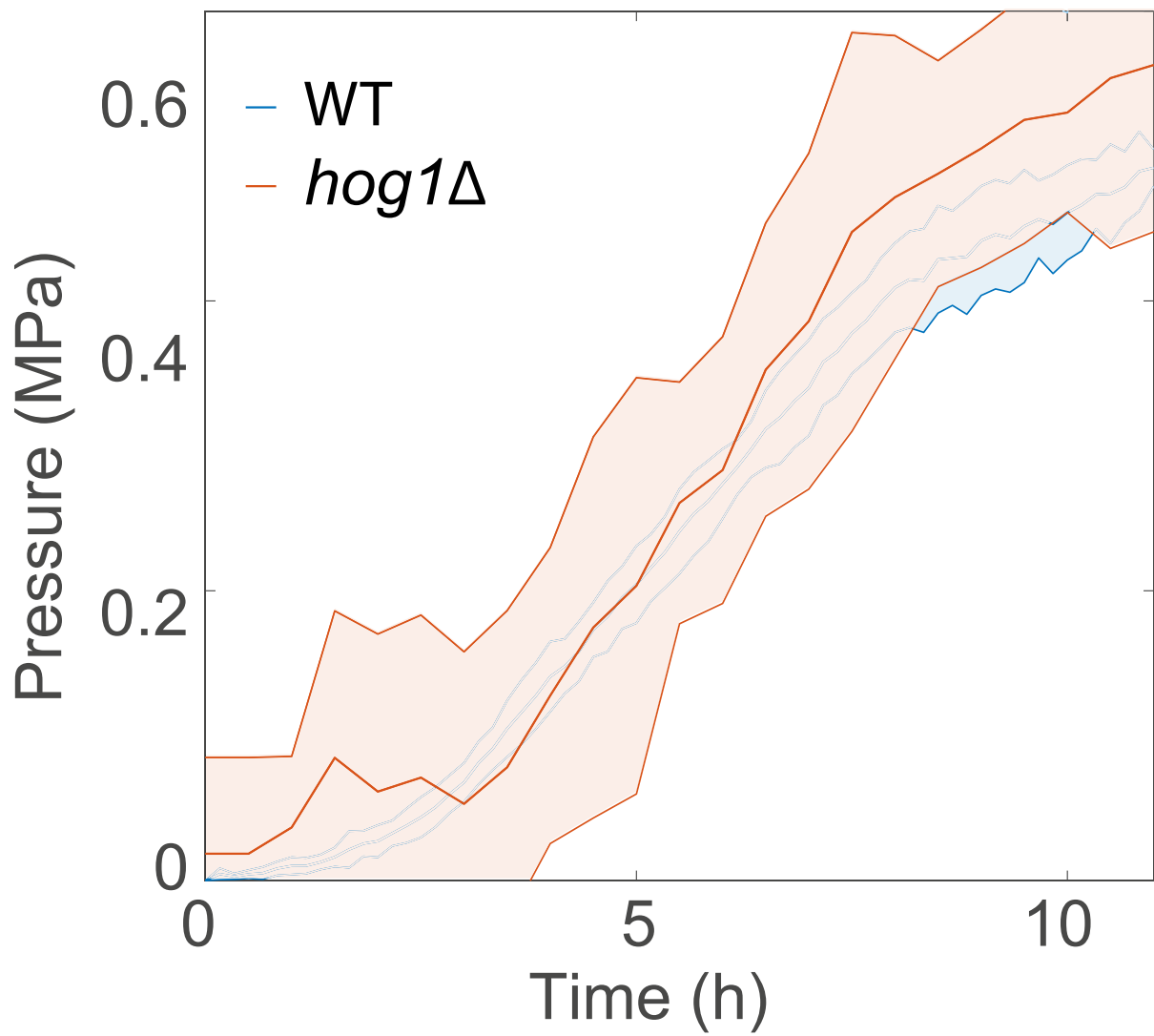
Extended Data Fig. 6 | Induction time of P_{ADH2} -mCherry. The induction time is plotted as a function of time. Inset: induction time plotted as a function of growth rate.



Extended Data Fig. 7 | Protein production rate as a function of GIP. In orange: data from the P_{ADH2} -*mCherry* promoter. In blue: data from the P_{HIS3} -*GFP* promoter.

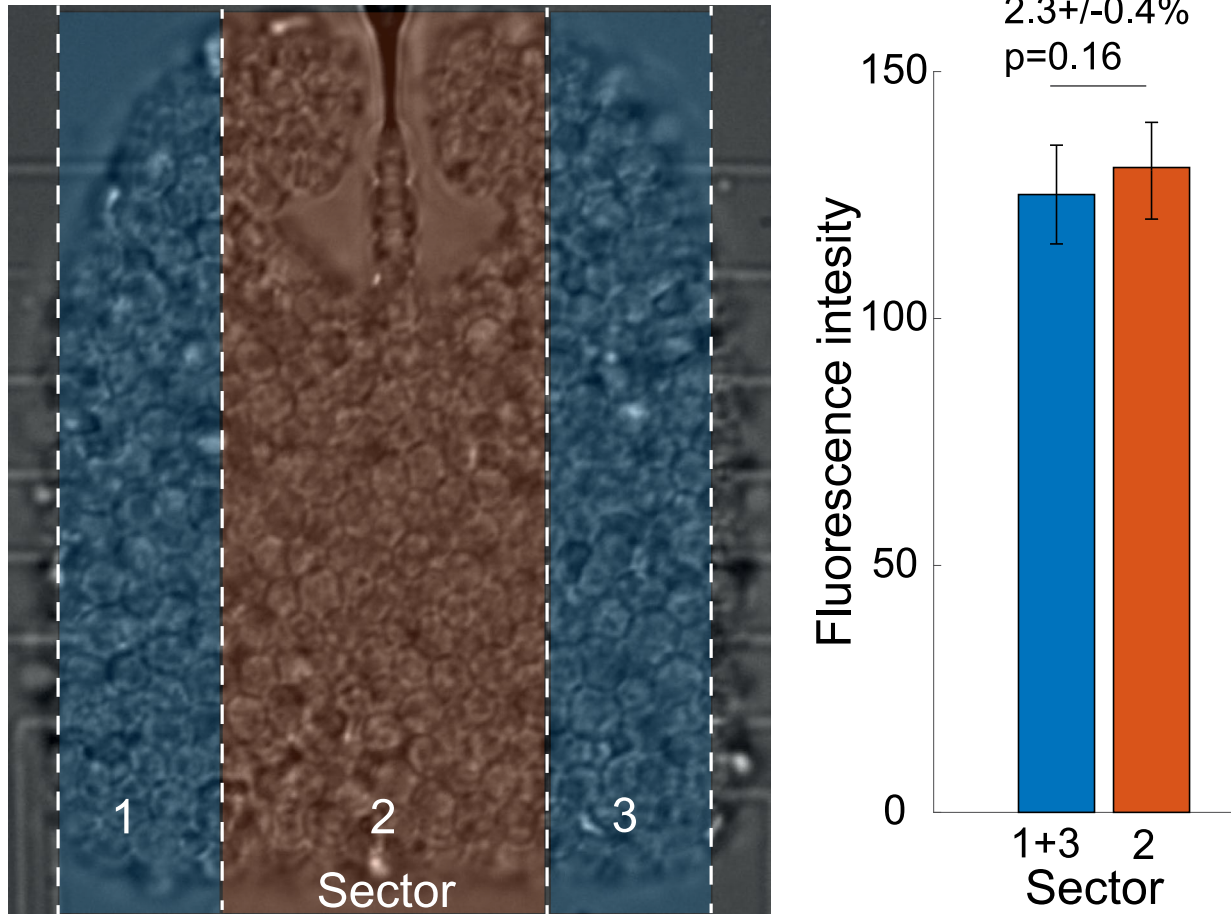


Extended Data Fig. 8 | Laser ablation experiments and calibration of turgor pressure. **a.** We used a high-intensity laser pulse to make a hole in a cell, forcing its deflation. The cell radius changes as a function of turgor pressure, cell wall elasticity, and thickness of the cell wall. **b.** Cells were punctured with a laser, resulting in a decrease in cell radius proportional to turgor pressure. The similar decrease in radius of WT and *hog1Δ* cells indicates that, absent osmotic perturbation, these cells develop similar amounts of turgor pressure. The decrease in radius of osmotically compressed ($c = 1\text{ M}$ sorbitol) *hog1Δ* cells indicates that these cells are still pressurized, albeit to a reduced extent. **c.** We used transmission electron microscopy to measure the cell wall thickness. **d.** We performed AFM experiments, using small deformations (below $0.2\ \mu\text{m}$) to extract the effective elasticity of the cell. This elasticity provided a mathematical function of turgor pressure, cell wall elasticity, and cell wall thickness.



Extended Data Fig. 9 | Growth induced pressure as a function of time. In blue, for the WT cells. In orange, for the *hog1Δ* cells.

P=0.4 MPa before *pADH2-mCherry* induction



Extended Data Fig. 10 | Measurement of the fluorescence intensity in the center versus the edge of the chamber prior to induction of P_{ADH2} -*mCherry*. The data shows an insignificant (p -value = 0.16) 2.3% difference.